


Cite this: *RSC Adv.*, 2021, 11, 9731

Nanochannel-based heterometallic {Zn^{II}Ho^{III}}–organic framework with high catalytic activity for the chemical fixation of CO₂†

Tao Zhang,^{ab} Hongtai Chen,^a Hongxiao Lv,^{ID a} Qiaoling Li^{*a} and Xiutang Zhang^{ID *a}

The exquisite combination of Zn^{II} and Ho^{III} generated the highly robust [ZnHo(CO₂)₆(OH)₂]-based heterometallic framework of {[ZnHo(TDP)(H₂O)]·5H₂O·3DMF}_n (NUC-30, H₆TDP = 2,4,6-tri(2',4'-dicarboxyphenyl)pyridine), which featured outstanding physicochemical properties, including honeycomb nanochannels, high porosity, large specific surface area, the coexistence of highly open Lewis acid–base sites, good thermal and chemical stability, and resistance to most organic solvents. Due to its extremely unsaturated metal tetra-coordinated Zn(II) ions, hepta-coordinated Ho(III) and high faveolate void volume (61.3%), the conversion rate of styrene oxide and CO₂ into cyclic carbonates in the presence of 2 mol% activated NUC-30 and 5 mol% *n*-Bu₄NBr reached 99% under the mild conditions of 1.0 MPa and 60 °C. Furthermore, the luminescence sensing experiments proved that NUC-30 could be used as a fast, sensitive and highly efficiency sensor for the detection of Fe³⁺ in aqueous solution. Therefore, these results prove that nanoporous MOFs assembled from pyridine-containing polycarboxylate ligands have wide applications, such as catalysis and as luminescent materials.

Received 22nd January 2021
Accepted 15th February 2021

DOI: 10.1039/d1ra00590a

rsc.li/rsc-advances

Introduction

Porous metal–organic frameworks (MOFs), as a booming family of organic–inorganic hybrid materials, have aroused much interest owing to their potential applications as heterogeneous catalysts, gas separation and storage materials, biomedical and chemical sensors, electrochemical microelectrodes, *etc.*¹ With the development of technology and social advancement, the highly optimized synthesis of targeted MOFs has been adopted and applied stepwise by combining functionalized organic linkers and special metal clusters to realize excellent functional characteristics including inherent porosity, large surface area, and active sites.² Thus far, numerous MOFs have been widely applied as a type of effective separation and catalytic material for the separation and chemical conversion of CO₂, which has created the serious problem of global warming because of excessive emissions from modern enterprises and motorized tools.³ Particularly, the mild reaction conditions of low temperature and pressure utilizing MOF catalysts are incomparable with other hetero- and homogeneous catalysts, for instance, zeolites, inorganic metal salts or oxides, ionic liquids, amine aqueous solutions, and polymerized organics.⁴

Furthermore, MOFs (*e.g.*, MOF-74/CPO-27 series),⁵ as a type of organic–inorganic hybrid material with marvelous structural adaptability, feature the excellent characteristics of high specific surface area and synergistic micropore size, consequently leading to a better unique adsorption performance for CO₂. In particular, the MOF-74 series of modified M₂(dobpdc) (dobpdc = 4,4'-diphenyl-3,3'-dicarboxylate) has been functionalized with diamine to exhibit excellent CO₂ absorption and selectivity under humid conditions, thus eliminating the water limitation.⁶ For instance, in traditional aqueous amine solutions, the diamine-grafted M₂(dobpdc) series fully demonstrates the advantage of Lewis acid–base sites, and thus CO₂ molecules can react with amines to form ammonium carbamate or bicarbonates. Therefore, due to the lower renewable energy cost from solid materials, diamine-appended M₂(dobpdc) materials with high working ability and energy efficiency are very promising candidates for CO₂ capture. Moreover, to promote the selective adsorption capacity of CO₂ in terms of kinetics and thermodynamics, research interest on MOFs at present is concentrated on their performance optimization by designing functional organic ligands to adjust their pore size, increasing open metal sites to improve their adsorption affinity for CO₂, and improving their thermal and chemical stability (*e.g.*, water resistance).⁷

Among the reported MOFs, Zn²⁺ ions, as one type of d-block metal ions and potential strong Lewis acid, have been paid close attention due to their distinctive characteristics including electronic configuration, binding energy, and charge distribution, which render various coupling affinities

^aNorth University of China, Taiyuan 030051, People's Republic of China. E-mail: qiaolingl@163.com; xiutangzhang@163.com

^bTaiyuan Institute of Technology, Taiyuan 030008, People's Republic of China

† Electronic supplementary information (ESI) available. CCDC 2002682. For ESI and crystallographic data in CIF or other electronic format see DOI: 10.1039/d1ra00590a



to multifarious donor atoms from ligands.⁸ Recently, reported Zn-MOFs based on tetra-coordinated Zn^{2+} ions with solvent-free channels displayed good selective adsorption performances for the guest molecules of CO_2 and catalyzed the chemical transformation of epoxides with CO_2 into the corresponding alkyl carbonates. This is because the exposed active Zn^{2+} ions act as a strong Lewis acid to polarize and activate CO_2 and the ring of ethylene oxide *via* coordination affinity.⁹ Thus, the self-assembly of nanoporous Zn-MOFs with the purpose of enhancing the amount of exposed active tetra- or penta-coordinated Zn^{2+} cations will become a research hotspot, especially for application in the selective separation or/and storage of guest molecules, catalysis for some specific reactions, and optics.¹⁰ Moreover, in the past decade, the research on the structure and chemical bond theory of Ln-MOFs has constantly increased, leading to a great deal of new research branches, such as catalysts, monomolecular magnets, magnetic refrigeration materials, and fluorescence recognition.¹¹ Thus far, for the reported Ln-MOFs, it has been exhibited that the coordination modes of Ln^{3+} can vary in a wide range with the largest coordination number of 12 due to the various orbital hybridization of $f^n d^{2+m} sp^3$ ($n = 0-3$, $m = 1-3$) by the electron orbitals of 6s, 6p, 5d, and 4f, which lead to a series of characteristics corresponding with the intrinsic structures.¹² Thus, although the Ln^{3+} ions included in the reported Ln-MOFs display octa- and nano-coordinated modes, they can still possess strong Lewis acidity and show strong affinity to small guest molecules with smaller steric resistance, such as CO_2 , SO_2 , N_xO_y , and H_2S . Recently, the metal-organic framework of $[\text{Eu}(\text{BTB})(\text{phen})]$ reported by Zhao and co-workers,^{12c} as the first example of Ln-MOFs for the fixation of CO_2 , displayed excellent catalytic activity for the chemical transformation of epoxides and CO_2 into carbonates under mild conditions, which further confirmed that the stable octa- and nano-coordinated state of Ln^{3+} ions could be viewed as a strong Lewis acid to polarize and activate approaching guest molecules.^{13,14}

In addition, some metal cations are also widely found in nature and living organisms, such as Fe^{3+} , which is one of the most crucial metal ions in the Earth's crust and biological systems, playing an important role in oxygen transportation, enzyme catalysis, cell metabolism, and DNA and RNA synthesis. A certain amount of Fe^{3+} is necessary to promote the formation of muscle and hemoglobin. Thus, insufficient or excessive Fe^{3+} can lead to physical diseases such as anemia, cirrhosis, heart failure, diabetes, cancer and decreased immunity. Excessive Fe^{3+} in the body can lead to neurodegenerative diseases, such as Alzheimer's disease and Parkinson's disease. Moreover, Fe^{3+} is a common inorganic pollutant in the aquatic environment, which can cause perpetual damage to human health and living surroundings even at low concentrations. Consequently, studies on the effective detection of Fe^{3+} are particularly important. However, traditional analytical methods, such as ion mobility spectroscopy (IMS), inductively coupled plasma (ICP), X-ray dispersion, atomic absorption spectrometry, are generally expensive and time-consuming.¹⁵

Considering the above discussion and our recent research, heterometallic MOFs with a high porosity distribution were explored by employing the pyridine-containing ligand of 2,4,6-tri(2',4'-dicarboxyphenyl)pyridine (H_6TDP), which possesses the followed characteristics: (i) ample carboxyl groups to bridge multiple metal cations, which is beneficial for the formation of a three-dimensional architecture and (ii) the nitrogen atom of pyridine can serve as a Lewis base site, tending to polarize acidic molecules of CO_2 . Herein, we report a robust, double-walled, nano-channel heterometallic framework of $\{[\text{ZnHo}(\text{TDP})(\text{H}_2\text{O})] \cdot 2\text{DMF} \cdot 4\text{H}_2\text{O}\}_n$ (**NUC-30**), which is based on the exquisite combination of dinuclear $[\text{ZnHo}(\text{CO}_2)_6(\text{H}_2\text{O})]$ SBUs and TDP^{6-} ligands. Interestingly, the desolvated **NUC-30** not only possesses dual nanoscopic channels, high porosity and large specific surface area, but also coexisting Lewis acid-base sites, including 4-coordinated Zn^{2+} ions, 7-coordinated Ho^{3+} ions, uncoordinated carboxyl oxygen atoms, and $\text{N}_{\text{pyridine}}$ atoms. Thus, as expected, **NUC-30** displayed high catalytic activity in the cycloaddition of various epoxides into the corresponding alkyl carbonates. In addition, the luminescence sensing experiments proved that **NUC-30** can be used as a fast, sensitive and highly efficiency sensor for the detection of Fe^{3+} in aqueous solution.

Experimental

Materials and general methods

2,4,6-Tri(2',4'-dicarboxyphenyl)pyridine (H_6TDP) was obtained from Jinan Henghua Sci. & Tec. Co. Ltd and used as received without further refinement. Infrared (IR) spectra were measured using a TENSOR 27 spectrometer in the wavenumber range of 600–4000 cm^{-1} . Thermogravimetric analysis (TGA) was carried out using a TG-209F3 thermal analyzer at a heating rate of 10 $^\circ\text{C min}^{-1}$ under an Ar stream. The powder X-ray (PXRD) diffraction analysis of the complexes was performed on a Rigaku SmartLab (9 kW) diffractometer with $\text{Cu-K}\alpha$ radiation at room temperature at the scanning speed of 10 $^\circ \text{min}^{-1}$. The SEM-EDS images of **NUC-30** were observed on a JSM-7200F scanning electron microscope (SEM, JEOL) at an acceleration voltage of 10.0 kV. Fluorescence spectra were measured using a Hitachi F-4600 fluorescence spectrophotometer at room temperature. The cryogenic N_2 adsorption and adsorption-desorption isotherms of CO_2 at 273 K and 298 K were measured on an ASAP 2020 Plus instrument.

Preparation of NUC-30

A homogeneous solution of anhydrous zinc chloride (0.014 g, 0.10 mmol), Ho_2O_3 (0.019 g, 0.05 mmol), H_6TDP (0.034 g, 0.06 mmol), 7 mL DMF, 2 mL H_2O , and 0.2 mL HNO_3 in a 25 mL autoclave was heated at 110 $^\circ\text{C}$ for 4 days and then gradually cooled to room temperature at a rate of 10 $^\circ\text{C h}^{-1}$. Colourless crystals of **NUC-30** were collected by filtration and washed with DMF/ H_2O (yield: 82% based on H_6TDP). Anal. calcd for **NUC-30** ($\text{C}_{29}\text{H}_{11}\text{HoNO}_{13}\text{Zn}$): C, 42.91%; H, 1.36%; N, 1.72%. Found: C, 42.57%; H, 1.42%; N, 1.74%. IR (KBr pellet, cm^{-1}): 3422 (vs), 1604 (vs), 1373 (vs), 1105 (w), 1020 (w), 855 (w), 770 (s), 672 (w).



X-ray crystallography

The diffraction intensity data for **NUC-30** was obtained at 296(2) K using a Bruker Smart-APEX II CCD area detector (Mo-K α radiation, $\lambda = 0.071073$ nm) with graphite monochromated radiation. The reflection data was corrected for empirical absorption corrections and Lorentz and polarization effects. The structure was solved by direct methods and refined by full-matrix least-squares with the SHELXL package. All non-hydrogen atoms were refined anisotropically. Hydrogen atoms except those on water molecules were generated geometrically with fixed isotropic thermal parameters and included in the structure factor calculations. The block of SQUEEZE in PLATON was employed to eliminate the highly disordered solvent molecules. The crystallographic data and refinement parameters for **NUC-30** are listed in Table S1.† Selected bond lengths and angles for **NUC-30** are presented in Table S2.† Further details on the crystal structure investigations can be obtained from the Cambridge Crystallographic Data Centre, with the depository number CCDC-2002682 for **NUC-30**.

PXRD and thermal analyses

To detect the phase purity, the samples of **NUC-30** and H₆TDP were characterized *via* X-ray powder diffraction at the scanning speed of 10° min⁻¹ in the 2 θ range of 5–30°. As shown in Fig. S1,† the powder X-ray diffraction pattern of **NUC-30** after activation was almost the same as the simulated pattern. The IR spectra of **NUC-30** and H₆TDP were measured in the frequency range of 600–4000 cm⁻¹, as shown in Fig. S2.† The SEM-EDS images of **NUC-30** illustrated that C, O, N, Zn and Ho were evenly distributed on the crystal surface (Fig. S3†). The thermal stability of **NUC-30** was tested by thermogravimetric analysis (TGA) and the result is shown in Fig. S4.† According to the TGA curve, the first weight loss of 8.75% in the temperature range of 25–120 °C is consistent with the associated water molecules. The second weight loss in the range of 120–400 °C is ascribed to the solvent of DMF. The framework remained stable up to 400 °C, indicating that **NUC-30** exhibits high thermal stability.

Catalytic experiment operation

The activated sample of **NUC-30** was obtained by immersing the newly synthesized crystals into methanol for one week, during which methanol was replaced three times at ambient temperature. Subsequently, the filtered crystals were dried in a vacuum drying oven at 393 K for one day. The catalytic cycloaddition reactions were performed in a 25 mL stainless clave under the solvent-free conditions of 10 atm CO₂ gas and 2 mmol% heterogeneous catalyst **NUC-30**. The qualitative detection during the reactive process was monitored by gas chromatography and the transformed product was determined by ¹H NMR spectroscopy. At the end of the catalytic reaction, the heterogeneous catalyst **NUC-30** was retrieved through simple centrifugation separation after each reaction was complete, and then cleaned with strong polar solvent of DMF and volatile solvent of acetone in sequence.

Result and discussion

Description of the crystal structure

The single-crystal XRD analysis exhibited that **NUC-30** crystallizes in the trigonal system with the $R\bar{3}m$ space group and exhibits a honeycomb anionic structure with dual-channels, which is built on the exquisite combination of paddlewheel [ZnHo(CO₂)₆(H₂O)] SBUs and bifunctional ligands of TDP⁶⁻. Although both types of alternately arranged nano-channels (**I** and **II**) in **NUC-30** shaped by six rows of [ZnHo(CO₂)₆(H₂O)] SBUs have an equal amount of exposed active metal sites, they could be discriminated from their different functionalized inner surfaces with free carboxyl oxygen atoms (C=O) and coordinated aqueous molecules (H₂O). It is worth mentioning that **NUC-30** features outstanding physicochemical properties including honeycomb nanochannels, high porosity, large specific surface area, coexisting highly open Lewis acid-base sites, good thermal and chemical stability, and resistance to most organic solvents. In addition, the activated **NUC-30** with void volume (61.3%) consists of extremely unsaturated metal ions including tetra-coordinated Zn(II) and hepta-coordinated Ho(III), which render the host framework a promising heterogeneous catalyst for the chemical fixation of CO₂.

Specifically, the asymmetric unit of **NUC-30** contains half a crystallographically unique Zn(II) ion, half an Ho(III) ion, and half a TDP⁶⁻ ligand. Firstly, the Ho(1) ion is chelated by two α -carboxylic groups with the coordination mode of μ_2 - η^1 : η^1 located on the 2-position of the phenyl rings, which are arranged on the 2- and 6-positions of the pyridine in TDP⁶⁻. Afterwards, the Ho(1) ion is further bridged to the Zn(1) ion to form one paddle-wheel dinuclear SBU of [Zn(CO₂)₆] with the separate Ho(1)⋯Zn(1) distance of 4.04(9) Å by three other γ -carboxyl groups, two of which are provided by two benzene rings on the 2-position of pyridine and one on the 4-position of pyridine (Fig. 1a). In addition, the Zn(1) ion is coordinated by one 2-position carboxyl group from another TDP⁶⁻ ligand. Thus, the formation of one [ZnHo(CO₂)₆(H₂O)] SBU is facilitated by five TDP⁶⁻ ligands, each of which simultaneously connects five [ZnHo(CO₂)₆(H₂O)] SBUs to generate one three-dimensional structure with honeycomb-like nanochannels (Fig. 1b). Although the Ho(1) ion is linked by seven carboxyl oxygen atoms and one aqueous molecule to constitute a “twisted double hat tri-prism” geometry (Fig. S5a†), it is worth mentioning that the associated water molecules can be easily removed under the activation conditions. In addition, the Zn(1) ion is linked by four carboxyl oxygen atoms from four different TDP⁶⁻ ligands to form a tetrahedron (Fig. S5b†) with the Zn(1)–O bond length in the range of 1.918(2)–1.963(2) Å. Even more exciting is that the tetrahedral Zn(1) in a tetrahedral coordination geometry is a natural Lewis acid site.

It is worth noting that each six rows of [ZnHo(CO₂)₆(H₂O)] SBUs are alternately bridged by TDP⁶⁻ ligands to form two types of edge-sharing nanochannels, namely circular and hexagonal ones. The circular nanochannels (**I**) with a pore diameter of 9.18 Å are characterized by the associated water molecules on the Ho³⁺ cations, pointing vertically to the center of the



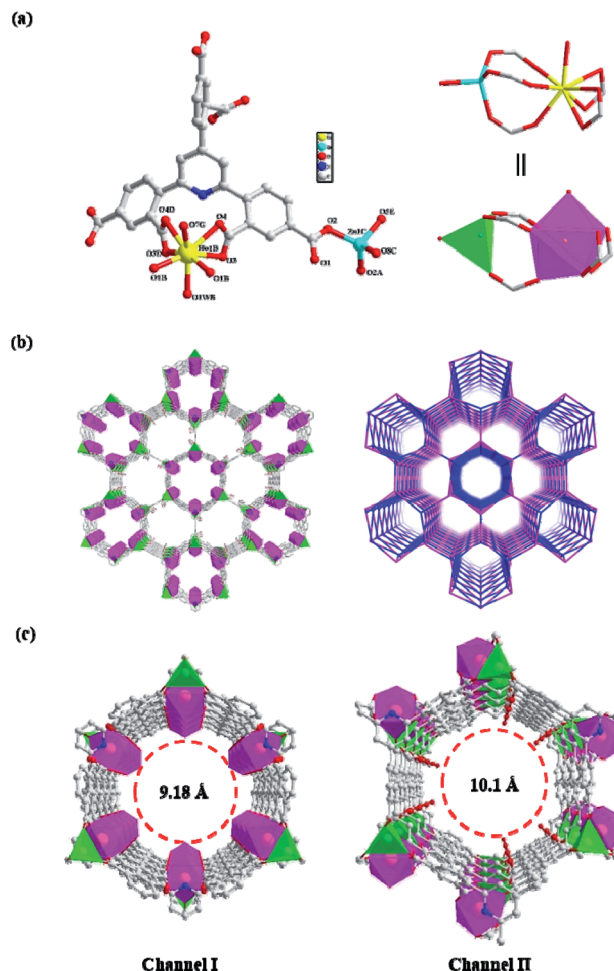


Fig. 1 (a) Structural building block of the TDP⁶⁻ ligand and [HoZn(CO₂)₆(H₂O)] (C, gray; O, red; Zn, cyan; Ho, yellow; N, blue; and H atoms are omitted for clarity). (b) 3D dual-channel framework of NUC-30 and its topology. (c) View of the 3D channel structure of NUC-30 along the *c*-axis.

nanochannel. However, the hexagonal nanochannels (II) with an aperture of 10.1 Å show that the free carboxyl oxygen atoms (C=O) reside on the inner walls, as shown in Fig. 1c. Therefore, channel I and channel II have completely different functionalized inner surfaces, except for the C–H organic panels and similar exposed metal parts on the walls.

Finally, for clarity, in the structure of NUC-30, the host framework was simplified as an fng-type framework with the Schläfli symbol of {4⁶·6⁴} as analyzed by TOPOS40. In the topology, the binuclear [HoZn(CO₂)₆(H₂O)] SBUs and trigeminal TDP⁶⁻ ligand are simplified as five-connected nodes, as shown in Fig. 1b.

Water resistance of NUC-30

Due to the obvious advantages of MOFs in gas-phase and liquid-phase adsorption fields, there is a lot of emphasis on their stability in the chemical environment. However, the low water resistance of most MOFs limits their application in the aqueous phase.¹⁵ Therefore, the water resistance of NUC-30 in different

aqueatic systems was analyzed. As shown in Fig. S6,[†] the PXRD spectra demonstrated that no structural collapse occurred after NUC-30 was soaked for 10 days at normal temperature, and even after soaking in boiling water for 72 h, which reflects its strong water resistance. This may be due to the change in the internal environment of its nanochannel by heterometallic doping, resulting in the strong hydrophobicity of the inner surface. The method of controlling the stability of MOFs by heterometallic doping also provides a new idea for improving the properties of porous metal–organic frameworks.

Gas adsorption studies

To explore the permanent porosity of NUC-30, crystal samples were soaked in methanol and dichloromethane separately three times a week, the solvent was changed every 24 h, and then dried under vacuum at 120 °C for 12 h. The PXRD pattern of the activated NUC-30 was consistent with the results of the X-ray single crystal diffraction data simulation, as shown in Fig. S7.[†] The adsorption capacity for N₂ at 77 K displayed that the total pore volume and calculated BET surface area of the activated NUC-30 were 0.38 cm³ g^{−1} and 701 m² g^{−1}, respectively. The adsorption–desorption isotherm of N₂ displayed a typical type-I adsorption configuration, and the hole distribution was in the range of 0.9–1.3 nm, as shown in Fig. S8.[†]

Due to the inherent structural advantages of the tubular nanochannels and the exposed high-density active metal sites of NUC-30, it has the potential to adsorb target molecules with quadrupole moments, and thus the adsorption of CO₂ was explored at 273 K and 298 K.^{16,17} As shown in Fig. 2, the maximum absorption of CO₂ at 273 K and 298 K was 93.44 cm³ g^{−1} and 64.99 cm³ g^{−1}, respectively, which are higher than that in the literature, such as for NUC-5, MOF-5, and Uio-66.¹⁸ Simultaneously, incomplete adsorption isotherms and CO₂ desorption lead to a moderate hysteresis loop, which confirms the strong interaction between the host and guest. Furthermore, in quantify the binding force between the CO₂ molecules and the framework of NUC-30, *Q*_{st} was calculated using the virial method with the resulting value at zero coverage being 25.8 kJ mol^{−1}, which implies that the adsorbed CO₂ molecules

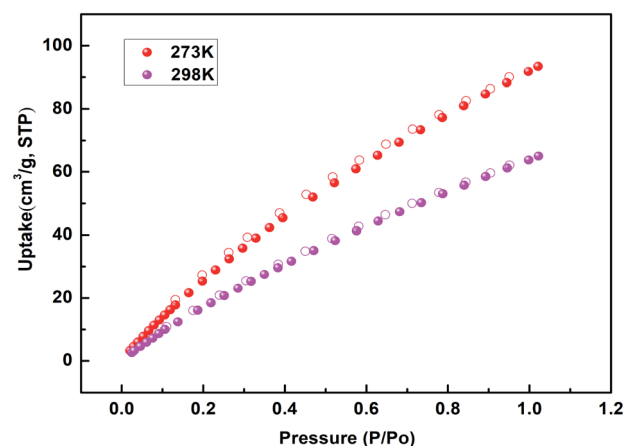


Fig. 2 CO₂ sorption isotherms of NUC-30 at 273 and 298 K.



can be easily released, allowing the host framework of **NUC-30** to be regenerated, as shown in Fig. S9.†

Catalytic cycloaddition of CO₂ and epoxides

On account of the abovementioned characteristics including highly exposed metal cations, highly partitioned functionalized nanochannels, large specific surface area, and good trapping performance of CO₂, the catalytic efficiency of **NUC-30** was tested for the chemical transformation of epoxides with CO₂ under comparatively mild conditions into cyclic carbonates, which is viewed as a bifunctional reaction for synergistically solving the energy crisis and reducing the amount of greenhouse gases.¹⁹ As illustrated in Table 1, 1,2-epoxypropane was selected as a model to explore the effects of different reaction conditions on the conversion of propylene oxide from CO₂ to propylene carbonate, and the obtained products were determined by ¹H NMR and GC-MS spectroscopy. Throughout the experimental process, the amount of **NUC-30** was set at 1.0 mol%. Entry 1 in Table 1 shows that the yield was 13% only in the presence of only solvation-free **NUC-30** at room temperature, while the co-catalyst Bu₄NBr under similar reaction conditions had a yield of 6% (entry 2). In contrast, as can be seen from entry 3, when 1.0 mol% **NUC-30** and 2.5 mol% Bu₄NBr were used simultaneously, the yield reached 49%, which proved that **NUC-30** and Bu₄NBr possessed completely different catalytic efficiency for the second-order reaction of cycloaddition from epoxides with CO₂. In addition, with an increase in temperature, the yield increased correspondingly, and the final yield reached 99% after 24 h at 60 °C (entry 6). However, when the amount of Bu₄NBr was doubled and **NUC-30** remained unchanged, the yield increased to 98% within 8 h at 60 °C (entry 10). Furthermore, as shown in entries 1 and 2, the

unsatisfactory results obtained by employing single **NUC-30** or *n*-Bu₄NBr demonstrated that the active open metal sites of **NUC-30** and anions of Br[−] played different roles during the cycloaddition reaction of CO₂ and epoxides. Therefore, the optimal reaction conditions used for subsequent experiments were quantified as 1.0 mol% **NUC-30** catalyst, 5 mol% *n*-Bu₄NBr co-catalyst, and 1.0 MPa CO₂ at 60 °C for 8 h. Compared with the recently reported MOF-based catalysts,²⁰ **NUC-30** showed a superior catalytic performance in terms of reaction conditions (Table S4†), which should be attributed to its intrinsic characteristics of active metal sites (Zn^{II} and Ho^{III}), uncoordinated pyridine and carboxyl oxygen atoms, and unimpeded void space. Furthermore, besides the synergistic catalytic effect of **NUC-30** and *n*-Bu₄NBr, the reaction temperature plays a key role during the cycloaddition process.

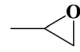
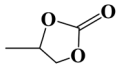
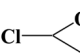
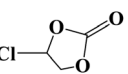
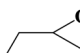
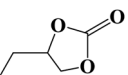
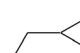
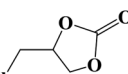
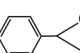
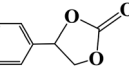
Under the established optimal reaction conditions including 20 mmol epoxide, 1.0 mol% **NUC-30**, 5 mol% *n*-Bu₄NBr, and 10 atm CO₂ at 60 °C for 8 h, a series of epoxide derivatives with typical substitutes was used to check the catalytic universality of **NUC-30**. As demonstrated in Table 2, the activated **NUC-30** exhibited significant catalytic activity for all the chosen substrates with yields higher than 96% under the set reaction conditions, except for styrene oxide with the relatively high boiling point of 194 °C, which may have limited its activity and rendered the final yield lower at the low temperature of 60 °C. The comparison of entries of 1–4 exhibited that epoxides with single electron-withdrawing groups are more likely to undergo

Table 1 Cycloaddition reaction of CO₂ with styrene oxide under various conditions^a

Entry	NUC-30 (mol%)	<i>n</i> -Bu ₄ NBr (mol%)	<i>T</i> (°C)	<i>t</i> (h)	Yield ^b (%)
1	1.0	0	25	24	13
2	0	2.5	25	24	6
3	1.0	2.5	25	24	49
4	1.0	2.5	40	24	72
5	1.0	2.5	50	24	85
6	1.0	2.5	60	24	99
7	1.0	5.0	60	2	41
8	1.0	5.0	60	4	65
9	1.0	5.0	60	6	88
10	1.0	5.0	60	8	98

^a Reaction conditions: 20 mmol propylene oxide, solvent free, CO₂ (10 atm). ^b Checked by ¹H NMR and GC-MS spectroscopy with *n*-dodecane as the internal standard.

Table 2 Cycloaddition reaction of CO₂ and various epoxides with **NUC-30** as the catalyst^a

Entry	Epoxide	Product	Yield ^{a,b} (%)	Selectivity (%)
1			99	>99
2			99	>99
3			98	>99
4			96	>99
5			92	>99

^a Reaction conditions: substrate (20 mmol), *n*-Bu₄NBr (5 mol%), **NUC-30** catalyst (1.0 mol% based on the Zn metal center), CO₂ (10 atm), 60 °C, and 12 h. ^b Determined by GC/MS with *n*-dodecane as the internal standard.



the cycloaddition reaction, which should be attributed to the fact that the electron absorption effect can effectively reduce the electron density of ethylene oxide. Furthermore, by comparing entries 1–4 and 5, it is clear that steric hindrance has a great influence on the cycloaddition reaction, which is consistent with the existing similar reactions catalyzed by porous MOFs.^{21,22} According to our hypothesis, the reason for this is that the larger substituents on the epoxides not only affect the convenience of their access to the nanocages, but also reduce the opportunity of interaction with the active sites. Moreover, compared to the reported porous MOF-based catalysts of **MOF-205(S)**,^{23a} **MMCF-2**,^{23b} and **Hf-Nu-1000**,^{23c} **NUC-30** exhibits superior catalytic efficiency, which should be ascribed to the contribution of the $[\text{ZnHo}(\text{CO}_2)_6(\text{H}_2\text{O})]$ units on the surface of its channels based on the clarified reaction mechanism. During the reaction process, the principle of catalysis is to reduce the reaction energy level and accelerate the reaction process by polarizing the reactants of epoxides and CO_2 .

The post-treatment including recovery and cyclic utilization for a proposed catalyst is one of the most important factors for evaluating its practical application besides excellent catalytic performance. Therefore, the ten-fold amplification reaction based on the optical conditions with 1,2-epoxypropane as the substrate by employing 500 mg **NUC-30** was repeated 5 times, during which **NUC-30** was recycled by filtration after each cycle and directly reused for the next cycle. When the fifth cycle was completed, the recovered sample of **NUC-30** was rinsed with dichloromethane, and subsequently vacuum dried, leaving a weight of 482 mg with the loss of 3.6%. The ICP analysis of the reaction solution showed that there was only a trace amount of Zn(II) ($\approx 0.027\%$) and Ho(III) ($\approx 0.018\%$) ions leached from the host framework. Notably, the catalytic effect of **NUC-30** was almost identical during the five cycles, which was confirmed by the transformation yield, as shown in Fig. S10.† Simultaneously, the PXRD pattern of the recovered **NUC-30** sample after five experimental runs was basically consistent with the original pattern, indicating that the structural integrity of **NUC-30** was still intact (Fig. S11†). As shown in Fig. S12,† the catalytic reaction was close to inactive after the catalyst was separated from the reaction system for a period of time, which confirmed the catalytic activity of **NUC-30**.

Given the clarified structure of **NUC-30** and recently published studies,^{6,23} the speculated catalytic mechanism is shown in Fig. 3. Primarily, the oxygen atom of the selected epoxide interacts with the open zinc sites on the inner wall of the nanotubular channel to decrease the original structural stability of the epoxide ring. Consequently, the bromide atom of TBAB poses nucleophilic attack on the less hindered carbon atom of the activated epoxide to generate one intermediate alkylcarbonate anion, which tends to launch an attack to the neighbouring polarized CO_2 molecule caught by the Lewis-acid metal sites in the nanochannel. Hence, it can be inferred that the whole process of cycloaddition can be boosted by coordination *via* the weak Lewis acidic–basic interactions involved in the porous framework.

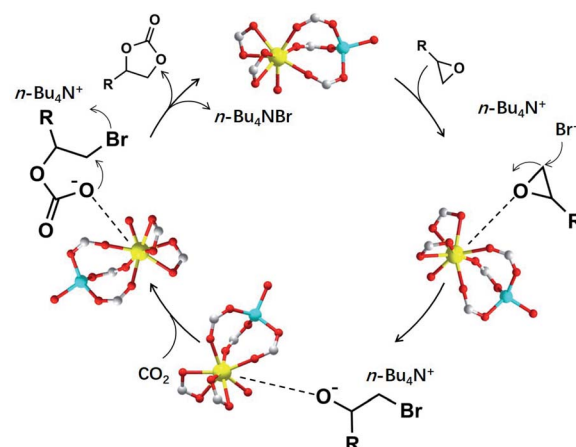


Fig. 3 Catalytic mechanism for the cycloaddition of epoxides with CO_2 .

Luminescence characteristic and sensing property

MOFs with d^{10} transition metal ions as constituents have been reported to be potential fluorescent materials in the field of optics. Consequently, the solid-state luminescence properties of the pure H_6TDP ligand and **NUC-30** at room temperature were studied, as shown in Fig. S13.† The maximum emission peaks of H_6TDP and **NUC-30** appeared at ~ 400 nm and ~ 410 nm, respectively. Compared with the H_6TDP ligand, the maximum emission of **NUC-30** has a weak red shift. Furthermore, due to their d^{10} electronic configuration, it is difficult to oxidize or reduce the Zn(II) and Ho(III) ions. Moreover, compared with the free H_6TDP , the emission of **NUC-30** was observed to be red-shifted, which is mainly due to the coordination effect between the ligand and metal ions. In addition, the excellent water-resistance of **NUC-30** makes it a potential luminescence probe to detect different metal ions.

Determination of Fe^{3+} cation

The investigation of the sensing ability of **NUC-30** for various cations was studied by adding 2 mg samples in 2 mL of 0.01 M

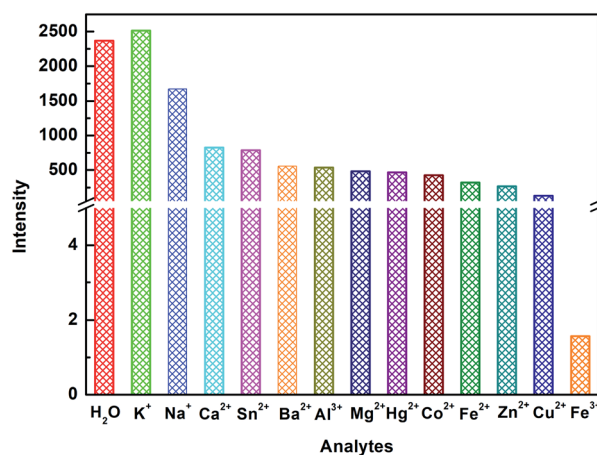


Fig. 4 Luminescence intensity of **NUC-30** at 397 nm in various cations.



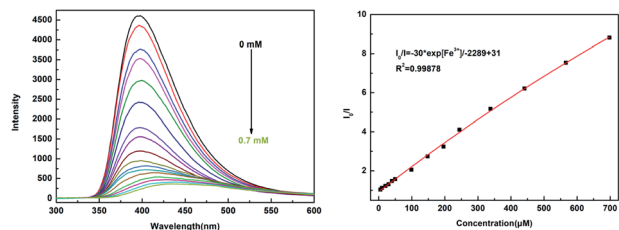


Fig. 5 (a) Luminescence spectra of the NUC-30@Fe³⁺ suspensions with the Fe³⁺ concentration varying from 0 to 0.75 mM (excited at 397 nm). (b) Plot of relative intensity vs. Fe³⁺ concentration.

aqueous solutions of twelve cations, M(Cl)_x (M = Na⁺, Zn²⁺, Co²⁺, Hg²⁺, K⁺, Ca²⁺, Ba²⁺, Cu²⁺, Mg²⁺, Al³⁺, Fe³⁺, Fe²⁺, and Sn²⁺) in water at room temperature. As seen in Fig. 4, the luminescent intensity of the Mⁿ⁺@CP suspensions varied with the different types of metal cations. The results exhibited that the Fe³⁺ cation has the best luminous quenching effects on NUC-30. The relationship between the concentration of Fe³⁺ cations and the luminescent intensity of the NUC-30 suspension was studied synchronously. As seen in Fig. 5, the fluorescent intensity of NUC-30 displayed an obvious quenching effect with the addition of Fe³⁺ solution. When the concentration of Fe³⁺ reached 0.7 mM, the quenching rate of NUC-30 increased to 97% (Fig. 5a). The non-linear Stern-Volmer curve for NUC-30@Fe³⁺ in aqueous system is consistent with the exponential equation of $I_0/I = -30 \times \exp[Fe^{3+}]/-2289 - 31$ for NUC-30 (Fig. 5b). In addition, as shown in Fig. S14,† NUC-30 had a high K_{SV} value of $2.413 \times 10^4 \text{ M}^{-1}$ for Fe³⁺ ions by fitting the experimental database in the low concentration range. Furthermore, according to the K_{SV} value and the standard deviation (δ), the detection minimum limit of NUC-30 for Fe³⁺ cations was determined to be 0.17 μM.

In addition, the infrared spectrum (IR) and PXRD patterns of the samples after the fluorescent experiment were consistent with the original samples, which shows that the structure of NUC-30 did not change (Fig. S15 and S16,† respectively). In addition, according to the structural characteristics of NUC-30 and the related studies on fluorescence recognition by MOFs,²⁴ the possible luminescence quenching mechanism of NUC-30 toward Fe³⁺ cations was further investigated. The ICP results showed that no Ho³⁺ ions were detected in the NUC-30@Ho³⁺ suspension after the luminescence experiments, indicating that the fluorescence quenching was not caused by ion exchange (Table S5†) and may be caused by the Fe³⁺ cations involved in the competitive absorption of the excitation light between them and the CPs, and the energy resonance transfer from the framework of NUC-30 to the Fe³⁺ cations.

Conclusions

By utilizing the ligand-directed synthetic strategy, the solvothermal self-assembly of Zn²⁺ and Ho³⁺ ions with the aid of the pre-designed H₆TDP generated the robust, double-walled, honeycomb material NUC-30, which exhibited excellent catalytic performances for the chemical transformation of various

epoxides into the corresponding carbonates under comparatively mild conditions of 10 atm CO₂ flow and 60 °C. Meanwhile, the water-resistant framework of NUC-30 could selectively and sensitively discriminate Fe³⁺ ions in aqueous solution. In fact, NUC-30 represents a class of emerging heterometallic nanoporous materials based on heterometallic binuclear SBUs. These materials not only feature the characteristics of dual tubular nanochannels, high porosity and specific surface area, but also possess tetra-coordinated transition metal ions and octa-coordinated rare earth ions. Although the ions of Zn²⁺ and Ho³⁺ were selected to construct the targeted model for the catalytic study on the chemical fixation of CO₂ by our group, other combinations of transition metal ions and octa-coordinated rare earth ions with the aid of H₆TDP can also be assembled for other specific functional studies in the future, such as optics and magnetism.

Conflicts of interest

The authors have no conflicts of interest to declare.

Acknowledgements

The work was supported by financial support from the Natural Science Foundation of China (21101097, 51573124), the Opening Foundation of Key Laboratory of Laser & Infrared System of Shandong University (2019-LISKFJJ-005), and the start-up funds of North University of China.

References

- (a) S. A. Montzka, E. J. Dlugokencky and J. H. Butler, *Nature*, 2011, **476**, 43–50; (b) J. D. Shakun, P. U. Clark, F. He, S. A. Marcott, A. C. Mix, Z. Y. Liu, B. Otto-Bliesner, A. Schmittner and E. Bard, *Nature*, 2012, **484**, 49–54; (c) P. Lanzafame, G. Centi and S. Perathoner, *Chem. Soc. Rev.*, 2014, **43**, 7562–7580; (d) Y. Wang, J. Ding, Y. Wang, X. Zhou, Y. Cao, B. Ma, J. Li, X. Wang, T. Seto and Z. Zhao, *J. Mater. Chem. C*, 2019, **7**, 1792–1820; (e) T. Yuan, T. Meng, P. He, Y. Shi, Y. Li, X. Li, L. Fan and S. Yang, *J. Mater. Chem. C*, 2019, **7**, 6820–6835; (f) V. Amoli, S. Y. Kim, J. S. Kim, H. Choi, J. Koo and D. H. Kim, *J. Mater. Chem. C*, 2019, **7**, 14816–14844; (g) S. Zhao and R. Jin, *ACS Energy Lett.*, 2018, **3**, 452–462.
- (a) A. Goepfert, M. Czaun, G. K. Surya Prakash and G. A. Olah, *Energy Environ. Sci.*, 2012, **5**, 7833–7853; (b) H. Wang, Z. Zhang, H. Wang, L. Guo and L. Li, *Dalton Trans.*, 2019, **48**, 15970–15976; (c) E. S. Sanz-Pérez, C. R. Murdock, S. A. Didas and C. W. Jones, *Chem. Rev.*, 2016, **116**, 11840–11876; (d) M. Z. Jacobson, *Energy Environ. Sci.*, 2009, **2**, 148–173; (e) D. M. Fernandes, A. F. Peixoto and C. Freire, *Dalton Trans.*, 2019, **48**, 13508–13528.
- (a) J. Yang, X. Wang, Y. Qu, X. Wang, H. Huo, Q. Fan, J. Wang, L. M. Yang and Y. Wu, *Adv. Energy Mater.*, 2020, **10**(36), 2001709; (b) J. H. Liu, L. M. Yang and E. Ganz, *J. Mater. Chem. A*, 2019, **7**, 3805–3814; (c) J. Liu, L. M. Yang and E. Ganz, *ACS Sustainable Chem. Eng.*, 2018, **6**, 15494–15502;



- (d) J. H. Liu, L. M. Yang and E. Ganz, *J. Mater. Chem. A*, 2019, 7, 11944–11952; (e) J. H. Liu, L. M. Yang and E. Ganz, *RSC Adv.*, 2019, 9, 27710–27719; (f) J. H. Liu, L. M. Yang and E. Ganz, *Energy Environ. Mater.*, 2019, 2, 193–200.
- 4 (a) S. Wang, K. Song, C. Zhang, Y. Shu, T. Li and B. Tan, *J. Mater. Chem. A*, 2017, 5, 1509–1515; (b) F. Guo and X. Zhang, *Dalton Trans.*, 2020, 49, 9935–9947; (c) S. Li, L. Zhang, Y. Lan, K. P. O'Halloran, H. Ma and H. Pang, *Nat. Commun.*, 2020, 11(1–10), 497; (d) S. Luo, Z. Zeng, G. Zeng, Z. Liu, R. Xiao, P. Xu, H. Wang, D. Huang, Y. Liu, B. Shao, Q. Liang, D. Wang, Q. He, L. Qin and Y. Fu, *J. Mater. Chem. A*, 2020, 8, 6434–6470; (e) L. Shi, Z. Li, L. Ju, A. Carrasco-Pena, N. Orlovskaya, H. Zhou and Y. Yang, *J. Mater. Chem. A*, 2020, 8, 1059–1065.
- 5 (a) Z. Ma, P. Li, L. Ye, Y. Zhou, F. Su, C. Ding, H. Xie, Y. Bai and P. K. Wong, *J. Mater. Chem. A*, 2017, 5, 24995–25004; (b) S. Luo, X. Li, M. Wang, X. Zhang, W. Gao, S. Su, G. Liu and M. Luo, *J. Mater. Chem. A*, 2020, 8, 5647–5654; (c) L. Sun, Y. Yun, H. Sheng, Y. Du, Y. Ding, P. Wu, P. Li and M. Zhu, *J. Mater. Chem. A*, 2018, 6, 15371–15376; (d) H. Zhang, L. M. Yang and E. Ganz, *ACS Sustainable Chem. Eng.*, 2020, 8, 14616–14626; (e) H. Zhang, L. M. Yang, H. Pan and E. Ganz, *Cryst. Growth Des.*, 2020, 20, 6337–6345.
- 6 (a) T. M. McDonald, W. R. Lee, J. A. Mason, B. M. Wiers, C. S. Hong and J. R. Long, *J. Am. Chem. Soc.*, 2012, 134, 7056–7065; (b) H. Zhang, C. Shang, L. M. Yang and E. Ganz, *Inorg. Chem.*, 2020, 59, 16665–16671; (c) H. Zhang, L. M. Yang and E. Ganz, *ACS Appl. Mater. Interfaces*, 2020, 12, 18533–18540; (d) H. Zhang, L. M. Yang, H. Pan and E. Ganz, *Phys. Chem. Chem. Phys.*, 2020, 22, 24614–24623; (e) H. Zhang, X. Zheng, L. M. Yang and E. Ganz, *Inorg. Chem.*, 2021, 60, 2656–2662.
- 7 (a) Y. Sun, X. Jia, H. Huang, X. Guo, Z. Qiao and C. Zhong, *J. Mater. Chem. A*, 2020, 8, 3180–3185; (b) R. Babu, R. Roshan, Y. Gim, Y. H. Jang, J. F. Kurisingal, D. W. Kim and D. W. Park, *J. Mater. Chem. A*, 2017, 5, 15961–15969; (c) L. Huang, B. Li, B. Su, Z. Xiong, C. Zhang, Y. Hou, Z. Ding and S. Wang, *J. Mater. Chem. A*, 2020, 8, 7177–7183; (d) X. L. Lv, L. H. Xie, B. Wang, M. Zhao, Y. Cui and J. R. Li, *J. Mater. Chem. C*, 2018, 6, 10628–10639; (e) H. Zhang, L. M. Yang and E. Ganz, *Langmuir*, 2020, 36, 14104–14112.
- 8 (a) F. Schönfeld, L. V. Meyer, F. Mühlbach, S. H. Zottnick and K. Müller-Buschbaum, *J. Mater. Chem. C*, 2018, 6, 2588–2595; (b) A. Yousaf, A. M. Arif, N. Xu, J. Zhou, C. Y. Sun, X. L. Wang and Z. M. Su, *J. Mater. Chem. C*, 2019, 7, 8861–8867; (c) H. Li, Q. Li and Z. Xu, *J. Mater. Chem. C*, 2019, 7, 2880–2885; (d) C. Li, W. Yang, X. Zhang, Y. Han, W. Tang, T. Yue and Z. Li, *J. Mater. Chem. C*, 2020, 8, 2054–2064; (e) F. Y. Yi, S. C. Wang, M. Gu, J. Q. Zheng and L. Han, *J. Mater. Chem. C*, 2018, 6, 2010–2018.
- 9 (a) Y. X. Zhang, B. X. Li, H. Lin, Z. Ma, X. T. Wu and Q. L. Zhu, *J. Mater. Chem. C*, 2019, 7, 6217–6221; (b) J. M. Liu, J. X. Hou, J. Liu, X. Jing, L. J. Li and J. L. Du, *J. Mater. Chem. C*, 2019, 7, 11851–11857; (c) Y. H. Luo, A. D. Xie, W. C. Chen, D. Shen, D. E. Zhang, Z. W. Tong and C. S. Lee, *J. Mater. Chem. C*, 2019, 7, 14897–14903.
- 10 (a) A. M. Kaczmarek and P. V. D. Voort, *J. Mater. Chem. C*, 2019, 7, 8109–8119; (b) S. Basu, S. Bhandari, U. N. Pan, A. Paul and A. Chattopadhyay, *J. Mater. Chem. C*, 2018, 6, 8205–8211.
- 11 (a) S. Jensen, K. Tan, W. Lustig, D. Kilin, J. Li, Y. J. Chabal and T. Thonhauser, *J. Mater. Chem. C*, 2019, 7, 2625–2632; (b) E. L. Zhou, C. Qin, D. Tian, X. L. Wang, B. X. Yang, L. Huang, K. Z. Shao and Z. M. Su, *J. Mater. Chem. C*, 2018, 6, 7874–7879; (c) E. Angioni, R. J. Marshall, N. J. Findlay, J. Bruckbauer, B. Breig, D. J. Wallis, R. W. Martin, R. S. Forgan and P. J. Skabara, *J. Mater. Chem. C*, 2019, 7, 2394–2400; (d) Y. Cheng, Y. Gao, H. Lin, F. Huang and Y. Wang, *J. Mater. Chem. C*, 2018, 6, 7462–7478.
- 12 (a) Y. J. Ma, S. D. Han, J. Pan, Y. Mu, J. H. Li and G. M. Wang, *J. Mater. Chem. C*, 2018, 6, 9341–9344; (b) W. P. Lustig, S. J. Teat and J. Li, *J. Mater. Chem. C*, 2019, 7, 14739–14744; (c) H. Xu, B. Zhai, C. S. Cao and B. Zhao, *Inorg. Chem.*, 2016, 55, 9671–9676; (d) J. Sun, P. Guo, M. Liu and H. Li, *J. Mater. Chem. C*, 2019, 7, 8992–8999; (e) L. Zhai, Z. X. Yang, W. W. Zhang, J. L. Zuo and X. M. Ren, *J. Mater. Chem. C*, 2018, 6, 7030–7041; (f) M. Gupta, D. De, K. Tomar and P. K. Bharadwaj, *Inorg. Chem.*, 2017, 56, 14605–14611.
- 13 (a) X. Wang, J. Liu, L. Zhang, L. Dong, S. Li, Y. Kan, D. Li and Y. Lan, *ACS Catal.*, 2019, 9, 1726–1732; (b) Q. Xu, B. Xu, H. Kong, P. He, J. Wang, T. Kannan, P. Ma, J. Wang and J. Niu, *Inorg. Chem.*, 2020, 59, 10665–10672; (c) M. Zhang, B. Liu, H. Zhang, C. Zhang, J. Wang and J. Niu, *Inorg. Chem.*, 2020, 59, 13733–13740; (d) D. Li, X. Ma, Q. Wang, P. Ma, J. Niu and J. Wang, *Inorg. Chem.*, 2019, 58, 15832–15840.
- 14 (a) C. Li, X. Tong, P. Yu, W. Du, J. Wu, H. Rao and Z. M. Wang, *J. Mater. Chem. A*, 2019, 7, 16622–16642; (b) Y. Wu, X. Song, S. Xu, Y. Chen, O. Oderinde, L. Gao, R. Wei and G. Xiao, *Dalton Trans.*, 2020, 49, 312–321; (c) J. Zhu, J. Liu, Y. Machain, B. Bonnett, S. Lin, M. Cai, M. C. Kessinger, P. M. Usov, W. Xu, S. D. Senanayake, D. Troya, A. R. Esker and A. J. Morris, *J. Mater. Chem. A*, 2018, 6, 22195–22203; (d) M. Wang, W. Zhong, S. Zhang, R. Liu, J. Xing and G. Zhang, *J. Mater. Chem. A*, 2018, 6, 9915–9921; (e) D. Ma, B. Li, K. Liu, X. Zhang, W. Zou, Y. Yang, G. Li, Z. Shi and S. Feng, *J. Mater. Chem. A*, 2015, 3, 23136–23142.
- 15 (a) X. P. Wang, W. M. Chen, X. Y. Li, C. Rajnák, Z. Y. Feng, M. Kurmoo, R. Boča, C. J. Jia, C. H. Tung and D. Sun, *Chem.–Eur. J.*, 2017, 23, 7990–7996; (b) W. M. Chen, X. L. Meng, G. L. Zhuang, Z. Wang, M. Kurmoo, Q. Q. Zhao, X. P. Wang, B. Shan, C. H. Tung and D. Sun, *J. Mater. Chem. A*, 2017, 5, 13079–13085; (c) D. Sun, G. G. Luo, N. Zhang, J. H. Chen, R. B. Huang, L. R. Lin and L. S. Zheng, *Polyhedron*, 2009, 28, 2983–2988; (d) D. Sun, Z. H. Yan, M. Liu, H. Xie, S. Yuan, H. Lu, S. Feng and D. Sun, *Cryst. Growth Des.*, 2012, 12, 2902–2907; (e) L. L. Han, T. P. Hu, K. Mei, Z. M. Guo, C. Yin, Y. X. Wang, J. Zheng, X. P. Wang and D. Sun, *Dalton Trans.*, 2015, 44, 6052–6061.
- 16 (a) X. Hu, L. Zhong, C. Shu, Z. Fang, M. Yang, J. Li and D. Yu, *J. Am. Chem. Soc.*, 2020, 142, 4621–4630; (b) X. Wu,



- D. G. Chen, D. Liu, S. H. Liu, S. W. Shen, C. I. Wu, G. Xie, J. Zhou, Z. X. Huang, C. Y. Huang, S. J. Su, W. Zhu and P. T. Chou, *J. Am. Chem. Soc.*, 2020, **142**, 7469–7479; (c) Y. X. Hu, X. Hao, L. Xu, X. Xie, B. Xiong, Z. Hu, H. Sun, G. Q. Yin, X. Li, H. Peng and H. B. Yang, *J. Am. Chem. Soc.*, 2020, **142**, 6285–6294; (d) Y. L. Wang, C. Li, H. Q. Qu, C. Fan, P. J. Zhao, R. Tian and M. Q. Zhu, *J. Am. Chem. Soc.*, 2020, **142**, 7497–7505; (e) O. Yang, F. Jacobson, P. Zhang and X. C. Huang, *J. Am. Chem. Soc.*, 2020, **142**, 6822–6832; (f) S. Yuan, L. Huang, Z. Huang, D. Sun, J. S. Qin, L. Feng, J. Li, X. Zou, T. Cagin and H. C. Zhou, *J. Am. Chem. Soc.*, 2020, **142**, 4732–4738.
- 17 (a) J. Liu, Y. Zhao, L. L. Dang, G. P. Yang, L. F. Ma, D. S. Li and Y. Y. Wang, *Chem. Commun.*, 2020, **56**, 8758–8761; (b) Y. P. Wu, J. W. Tian, S. Liu, B. Li, J. Zhao, L. F. Ma, D. S. Li, Y. Q. Lan and X. Bu, *Angew. Chem., Int. Ed.*, 2019, **58**, 12185–12189; (c) D. M. Su, J. Qu, Y. C. Hu, S. S. Yu, W. Z. Tang, Y. B. Liu, S. G. Ma and D. Q. Yu, *Chin. Chem. Lett.*, 2018, **19**, 845–848; (d) Z. Qin, W. Dong, J. Zhao, Y. Wu, Q. Zhang and D. Li, *Inorg. Chem. Front.*, 2018, **5**, 120–126.
- 18 (a) H. Chen, L. Fan, X. Zhang and L. Ma, *ACS Appl. Mater. Interfaces*, 2020, **12**, 27803–27811; (b) G. H. V. Bertrand, J. Dumazert, F. Sguerra, R. Coulon, G. Corre and M. Hamel, *J. Mater. Chem. C*, 2015, **3**, 7523; (c) X. Liu, *Front. Chem. Sci. Eng.*, 2020, **14**, 216–232; (d) J. H. Wei, J. W. Yi, M. L. Han, B. Li, S. Liu, Y. P. Wu, L. F. Ma and D. S. Li, *Chem.-Asian J.*, 2019, **14**, 3694–3701; (e) J. W. Tian, Y. P. Wu, Y. S. Li, J. H. Wei, J. W. Yi, S. Li, J. Zhao and D. S. Li, *Inorg. Chem.*, 2019, **58**, 5837–5843.
- 19 (a) X. Wang, B. Li, Y. P. Wu, A. Tsamis, H. G. Yu, S. Liu, Y. Zhao, Y. S. Li and D. S. Li, *Inorg. Chem.*, 2020, **59**, 4764–4771; (b) C. X. Yu, K. Z. Wang, X. J. Li, D. Liu, L. F. Ma and L. L. Liu, *Cryst. Growth Des.*, 2020, **20**, 5251–5260; (c) X. G. Yang, Z. M. Zhai, L. F. Ma and D. P. Yan, *ACS Cent. Sci.*, 2020, **6**, 1169–1178; (d) H. R. Fu, N. Wang, X. X. Wu, F. F. Li, Y. Zhao, L. F. Ma and M. Du, *Adv. Opt. Mater.*, 2020, **8**(13), 2000330; (e) C. X. Yu, F. L. Hu, J. G. Song, J. L. Zhang, S. S. Liu, B. X. Wang, H. Meng, L. L. Liu and L. F. Ma, *Sens. Actuators, B*, 2020, **310**, 127819; (f) J. Liu, G. P. Yang, J. Jin, D. Wu, L. F. Ma and Y. Y. Wang, *Chem. Commun.*, 2020, **56**, 2395–2398.
- 20 (a) Y. Zhao, Y. J. Wang, N. Wang, P. Zheng, H. R. Fu, M. L. Han, L. F. Ma and L. Y. Wang, *Inorg. Chem.*, 2019, **58**, 12700–12706; (b) Y. P. Wu, J. W. Tian, S. Liu, B. Li, J. Zhao, L. F. Ma, D. S. Li, Y. Q. Lan and X. Bu, *Angew. Chem., Int. Ed.*, 2019, **58**, 12185–12189; (c) Y. Zhao, X. G. Yang, X. M. Lu, C. D. Yang, N. N. Fan, Z. T. Yang, L. Y. Wang and L. F. Ma, *Inorg. Chem.*, 2019, **58**, 6215–6221; (d) Y. J. Cheng, R. Wang, S. Wang, X. J. Xi, L. F. Ma and S. Q. Zang, *Chem. Commun.*, 2018, **54**, 13563–13566; (e) Z. He, X. Zhao, X. Pan, Y. Li, X. Wang, H. Xu and Z. Xu, *RSC Adv.*, 2019, **43**, 25170–25176.
- 21 (a) X. P. Wang, W. M. Chen, H. Qi, X. Y. Li, C. Rajnák, Z. Y. Feng, M. Kurmoo, R. Boča, C. J. Jia, C. H. Tung and D. Sun, *Chem.-Eur. J.*, 2017, **23**, 7990–7996; (b) Z. Wang, X. Y. Li, L. W. Liu, S. Q. Yu, Z. Y. Feng, C. H. Tung and D. Sun, *Chem.-Eur. J.*, 2016, **22**, 6830–6836; (c) Z. Xu, L. L. Han, G. L. Zhuang, J. Bai and D. Sun, *Inorg. Chem.*, 2015, **54**, 4737–4743; (d) Z. H. Yan, X. Y. Li, L. W. Liu, S. Q. Yu, X. P. Wang and D. Sun, *Inorg. Chem.*, 2016, **55**, 1096–1101; (e) Y. Yuan, K. Sheng, S. Zeng, X. Han, L. Sun, I. Lončarić, W. Zhan and D. Di Sun, *Inorg. Chem.*, 2020, **59**, 5456–5462.
- 22 (a) Y. N. Liu, J. L. Hou, Z. Wang, R. K. Gupta, Z. Jagličić, M. Jagodić, W. G. Wang, C. H. Tung and D. Sun, *Inorg. Chem.*, 2020, **59**, 5683–5693; (b) F. Yu, B. Q. Ji, M. Jagodić, Y. M. Su, S. S. Zhang, L. Feng, M. Kurmoo, Z. Jagličić and D. Sun, *Inorg. Chem.*, 2020, **59**, 13524–13532; (c) X. Q. Liang, R. K. Gupta, Y. W. Li, H. Y. Ma, L. N. Gao, C. H. Tung and D. Sun, *Inorg. Chem.*, 2020, **59**, 2680–2688; (d) C. Ma, P. Wang, Z. Liu, C. Xin, S. Wang, J. Jia, P. Ma, J. Niu and J. Wang, *Inorg. Chem.*, 2020, **59**, 8690–8698; (e) Z. Liang, Y. He, Y. Qiao, P. Ma, J. Niu and J. Wang, *Inorg. Chem.*, 2020, **59**, 7895–7899.
- 23 (a) R. Babu, R. Roshan, A. C. Kathalikkattil, D. W. Kim and D. W. Park, *ACS Appl. Mater. Interfaces*, 2016, **8**, 33723–33731; (b) W. Y. Gao, Y. Chen, Y. Niu, K. Williams, L. Cash, P. J. Perez, L. Wojtas, J. Cai, Y. S. Chen and S. Ma, *Angew. Chem., Int. Ed.*, 2014, **53**, 2615–2619; (c) M. H. Beyzavi, R. C. Klet, S. Tussupbayev, J. Borycz, N. A. Vermeulen, C. J. Cramer, J. F. Stoddart, J. T. Hupp and O. K. Farha, *J. Am. Chem. Soc.*, 2014, **136**, 15861–15864; (d) V. Singh, S. Liu, P. Ma, M. G. B. Drew, J. Wang and J. Niu, *Inorg. Chem.*, 2020, **59**, 1125–1136; (e) J. He, J. Li, Q. Han, C. Si, G. Niu, M. Li, J. Wang and J. Niu, *ACS Appl. Mater. Interfaces*, 2020, **12**, 2199–2206; (f) N. Sun, C. Wang, H. Wang, X. Gao and J. Jiang, *ACS Appl. Mater. Interfaces*, 2020, **12**, 5649–56498.
- 24 (a) H. Lv, H. Chen, L. Fan and X. Zhang, *Dalton Trans.*, 2020, **49**, 14656–14664; (b) V. Gupta and S. K. Mandal, *Inorg. Chem.*, 2020, **59**, 4273–4281; (c) Z. F. Wu, E. Velasco, C. Shan, K. Tan, Z. Z. Zhang, Q. Q. Hu, K. Xing, X. Y. Huang and J. Li, *J. Mater. Chem. C*, 2020, **8**, 6820–6825; (d) D. Jiang, X. Yang, X. Zheng, L. Bo, T. Zhu, H. Chen, L. Zhang and S. Huang, *J. Mater. Chem. C*, 2018, **6**, 8513–8521; (e) B. Liu, M. Böckmann, W. Jiang, N. L. Doltsinis and Z. Wang, *J. Am. Chem. Soc.*, 2020, **142**, 7092–7099.

